High-density three-dimensional localization microscopy across large volumes

Wesley R Legant[1], Lin Shao[1], Jonathan B Grimm[1], Timothy A Brown[1], Daniel E Milkie[1,2], Brian B Avants[3,4], Luke D Lavis[1] & Eric Betzig[1]

Extending three-dimensional (3D) single-molecule localization microscopy away from the coverslip and into thicker specimens will greatly broaden its biological utility. However, because of the limitations of both conventional imaging modalities and conventional labeling techniques, it is a challenge to localize molecules in three dimensions with high precision in such samples while simultaneously achieving the labeling densities required for high resolution of densely crowded structures. Here we combined lattice light-sheet microscopy with newly developed, freely diffusing, cell-permeable chemical probes with targeted affinity for DNA, intracellular membranes or the plasma membrane. We used this combination to perform high–localization precision, ultrahigh–labeling density, multicolor localization microscopy in samples up to 20 μm thick, including dividing cells and the neuromast organ of a zebrafish embryo. We also demonstrate super-resolution correlative imaging with protein-specific photoactivable fluorophores, providing a mutually compatible, single-platform alternative to correlative light-electron microscopy over large volumes.

Localization microscopy methods allow the study of biological structures well below the optical diffraction limit[1]. However, despite their ability to localize fluorescent molecules in both two and three dimensions[2–4], the majority of applications have focused on the ventral surface or very thin (<1 μm) lamellar regions of adherent cells. Two challenges arise when localization microscopy is extended to thicker 3D samples. First, in order for single molecules to be localized, background signal from fluorescent emitters residing outside of the focal plane must be reduced through either limitation of the excitation volume or restriction of the specimen thickness. Oblique illumination[5], multifocal detection[6], temporal focusing[7,8] and selective-plane illumination[9] (SPIM) have all been used to attain high localization precision in thick samples. However, the region of activation and/or excitation in each case is thicker than the depth of focus of detection, leading to out-of-focus background and premature bleaching of activated molecules, and degrading both the attainable localization precision and the localization density.

This degradation of localization density is especially relevant because the second, often overlooked challenge for high-resolution 3D structural imaging is that the number of molecules required to adequately sample a given spatial frequency, and thus to resolve a structure of a given size, scales exponentially with the spatial dimension in which those structures are imaged (**Supplementary Notes 1–5**, **Supplementary Figs. 1–7** and **Supplementary Video 1**). This issue is often addressed by analogy to the Nyquist sampling theorem[1,10–18], which links optical resolution, localization density and spatial dimension in localization microscopy. By the Nyquist criterion, resolving a structure at 20-nm resolution would require the localization of up to 37,500 unique molecules within a 3D ($250 \times 250 \times 600$ nm) diffraction-limited volume in the worst-case scenario, where the volume is filled with structures at this scale. Even if such labeling densities could be achieved with conventional fluorescent proteins or antibodies without overexpression artifacts or a loss of labeling specificity, the on:off contrast ratio of the activated:nonactivated fluorophore would still have to be more than 40,000:1 in order for the one activated molecule to be accurately localized against the background of those remaining. Moreover, because localizations represent a stochastic sampling of the underlying molecular distribution, adequately sampling a given spatial frequency with sufficient signal to noise can require an order-of-magnitude increase in the number of molecules compared to what is strictly required according to the Nyquist criterion[19].

To address both challenges in thick specimens, we used lattice light-sheet (LLS) microscopy[10] to illuminate an approximately 1.1-μm-thick plane coincident with and similar in thickness to the depth of focus of our 1.1–numerical aperture (NA) detection objective (**Supplementary Note 6**). This ensured that only molecules near the focal plane were excited. To address the labeling density challenge, we combined this illumination scheme with point accumulation for imaging of nanoscale topography (PAINT) microscopy[20]. In PAINT microscopy, labels continually bind to the specimen throughout the imaging process, providing a continuous source of fluorescent molecules to label the structure (**Supplementary Video 2** and **Supplementary Note 7**).

We also introduce two new PAINT labels that selectively bind either to intracellular membranes or fluorogenically to DNA (**Supplementary Fig. 8** and **Supplementary Note 8**). We used this combination of confined planar illumination, stochastic binding and novel chemical probes to perform LLS-PAINT microscopy at high localization precision and high labeling density, in multiple colors, for samples up to 20 μm thick, including dividing cells and features at the periphery of small embryos.

RESULTS
The effect of localization density on structural imaging
Many studies use the Nyquist criterion (i.e., two unique molecular localizations per unit length) to incorporate the effect of localization density on resolution[1,10–18]. However, a 'sample' in the context of the Nyquist-Shannon sampling theorem is different from a localization event in localization microscopy (**Supplementary Note 1**): the former relates to periodic sampling of a scalar-valued function (for example, when digitizing an analog signal), whereas the latter involves stochastic, nonperiodic sampling and does not, in a single event, reveal the underlying molecular density at a given location. Rather, each 'event' is drawn from a probability distribution that is proportional to the underlying density of fluorophores[21], which themselves are usually only proxies for the often incompletely labeled endogenous molecular targets of true biological interest. When used for structural imaging, the task for localization microscopy then is to observe a sufficient number of localization events to resolve the underlying distribution or structure.

In light of this distinction, and to determine what density of localized molecules would be required to obtain a given resolution, we used both simplified periodic 1D and 2D signals (**Supplementary Note 1** and **Supplementary Figs. 1–4**) and experimentally relevant images of the actin cytoskeleton[22] (**Fig. 1**, **Supplementary Notes 2–5** and **Supplementary Figs. 5–7**). We used these signals and images as ground truth templates from which we simulated the stochastic molecular localization and image-reconstruction process used in localization microscopy. Our results suggest that accurately reconstructing the periodic signal of the ground truth functions and obtaining localization microscopy data that are qualitatively comparable to electron microscopy (EM) images of well-defined resolution can require a fivefold or greater increase in the number of molecules to be localized compared with what has previously been reported according to the Nyquist criterion. Therefore, in the rest of this paper, we report resolution using this fivefold-oversampling condition.

However, we stress the following: (1) these values are inferred lower bounds on the attainable resolution, (2) the resolution varies throughout the cellular volume, and (3) true resolution at any given point will further be influenced by the combination of labeling specificity for the target, linker length from the label to the target, the accuracy of drift correction (discussed below), the possibility of molecule diffusion in a single camera exposure (especially for PAINT probes), the spatial frequency content of the sample itself[21,23] and the desired level of certainty regarding the underlying molecular density[19].

3D localization microscopy of intracellular membranes
Screening of disparate rhodamine derivatives showed that azepanyl-rhodamine (AzepRh[24]) was an effective membrane stain (**Supplementary Fig. 8**). We used this probe to preferentially label the intracellular membranes throughout the 3D volume of an adherent, chemically fixed COS-7 cell (**Fig. 2a,b** and **Supplementary Videos 3** and **4**). We recorded nearly 150,000 3D volumes comprising more than 20 million 2D images acquired in 270-nm steps. From these images, we localized approximately 400 million individual molecules to a median CRLB (Cramer-Rao lower bound) precision of $8.9 \times 9.7 \times 41$ nm in the lateral and axial directions, corresponding to a full-width at half-maximum of $20.9 \times 22.8 \times 96.4$ nm for a point object (i.e., 2.35 times larger than the CRLB). Note that in LLS microscopy, the detection axis (denoted by z, and which has the poorest resolution) lies oblique to the coverslip (**Supplementary Fig. 9**). For ease of visualization, most images are displayed in a plane parallel to the coverslip and perpendicular to the coverslip's z (cz) axis; however, we note that this leads to blending of the high-precision lateral and low-precision axial localizations in the image. The resolution bounds inferred from the localization precision and labeling density varied in different regions of the sample. However, when we used a density criterion of fivefold oversampling relative to the Nyquist criterion, the 23,400–6,950 localizations per diffraction-limited volume here yielded a density-limited lower bound of 40–60-nm resolution throughout much of the cell (**Supplementary Video 4**). When combined with the anisotropic localization precision noted above, this resulted in inferred lower bounds on the overall resolution of approximately 45–64 nm in the lateral direction and 104–114 nm in the axial direction (**Supplementary Note 1**). Across the entire 6-μm depth of the cell, the super-resolved image displayed substantially higher resolution than a deconvolved diffraction-limited LLS image (**Fig. 2c–e** and

Figure 1 | The effect of labeling density in localization microscopy. (**a**) Electron micrograph of actin in the lamellapodia of an adherent cell. (**b**) Zoomed-in view of the outlined region in **a** plotted at an inferred resolution of 3 nm. (**c**) Binarized ground truth distribution of actin versus background. (**d**) Replotted ground truth image filtered to 31-nm resolution. (**e**) Simulated localization microscopy image plotted at 1× Nyquist density and 10-nm localization precision. This would be reported as having an identical 31-nm resolution assuming a requirement of 1× Nyquist sampling. (**f**) Simulated localization microscopy image plotted at fivefold greater localization density than in **e**. This would be reported as having a 31-nm resolution assuming a requirement for 5× oversampling compared to the Nyquist criterion (discussed further in **Supplementary Note 1**). Scale bars, 1 μm (**a**) or 500 nm (**b–f**). **a** and **b** reproduced with permission from ©1999 Svitkina and Borisy. *Journal of Cell Biology*. **145**:1009–1026. doi:10.1083/jcb.145.5.1009.
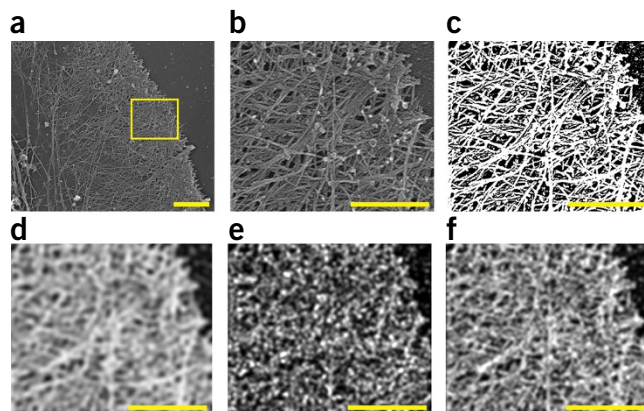
Figure 2 | Whole-cell 3D localization microscopy of intracellular membranes. (**a**) Maximum-intensity projection of a COS-7 cell imaged with LLS-PAINT microscopy using AzepRh. Note that this projection mixes the high-resolution x-axis with the low-resolution z-axis of the microscope (**Supplementary Fig. 9**) but is more natural for the specimen geometry. (**b**) Maximum-intensity projection of outlined region b in **a**. White arrows indicate both sheet-like and reticulated tubule morphology of the ER. Larger tubular structures are mitochondria. (**c**) Single 20-nm-thick orthoslice taken approximately 500 nm above the coverslip from outlined region c in **a**. The white arrow highlights a void in a tubular mitochondrion. (**d**) Single 20-nm-thick orthoslice parallel to and approximately 2.5 μm above the coverslip from the perinuclear region (region d) outlined in **a**. (**e**) 12.5-nm-thick orthoslice oriented perpendicular to the sample scan axis (s-axis; **Supplementary Fig. 9**), denoted by the dashed line in **a**. For comparison, **c**–**e** show orthoslices from both PAINT and deconvolved diffraction-limited LLS volumes from the same region. Scale bars, 5 μm (**a**) or 1 μm (**b**–**e**). Image post processing is described in the Online Methods. Also see **Supplementary Videos 3** and **4**.
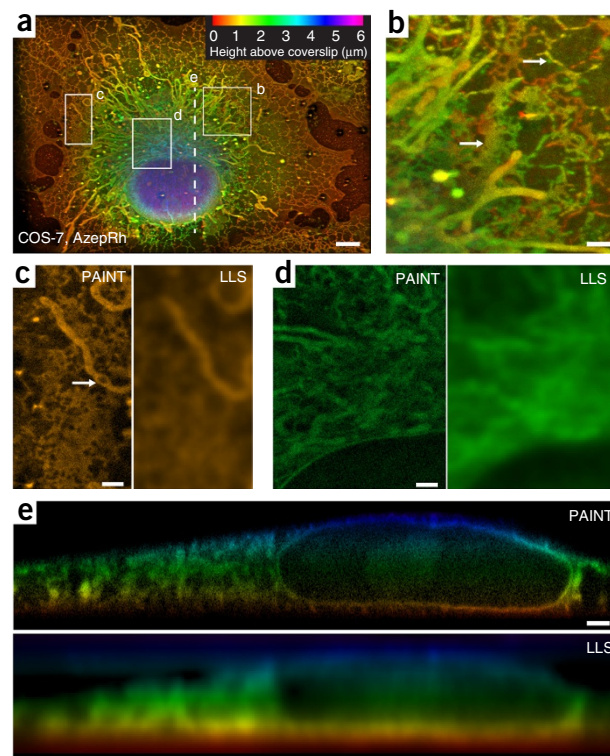
Supplementary Video 3), and several sections had features that could be clearly distinguished at ~70 nm and ~100 nm in the lateral and axial dimensions, respectively (**Supplementary Fig. 10**), which is consistent with these values.

Although AzepRh labels membranes of the endoplasmic reticulum (ER), mitochondria, Golgi and lysosomes (**Supplementary Figs. 11**–**14**), we were able to discriminate ER and mitochondria throughout most of the cell on the basis of their characteristic morphologies. We observed both reticulated tubules and flattened sheet-like ER structures in the peripheral lamella as well as throughout the 3D perinuclear volume (**Fig. 2b**). We also

observed an extensive tubular ER network immediately concentric to the outer nuclear envelope. Several mitochondria showed voids, similar to what has been observed previously with 2D live-cell localization microscopy and 3D structured illumination microscopy (SIM) using vital dyes[16,25,26] (**Fig. 2c**). Because of the label's ubiquitous staining pattern, the contrast achieved with LLS-PAINT microscopy using AzepRh resembles that in heavy metal–stain EM images. However, although its resolution is lower than that of EM in the plane of the coverslip, LLS-PAINT offers subdiffraction 3D resolution throughout whole cellular volumes without the need for mechanical sectioning.

Multicolor LLS-PAINT microscopy

In contrast to EM, PAINT microscopy allows for multicolor imaging via sequential staining with labels having affinity for different structures. To demonstrate this, we performed sequential imaging of a COS-7 cell stained with AzepRh (70,000 volumes, 91 million molecules) and wheat germ agglutinin–Alexa Fluor 555
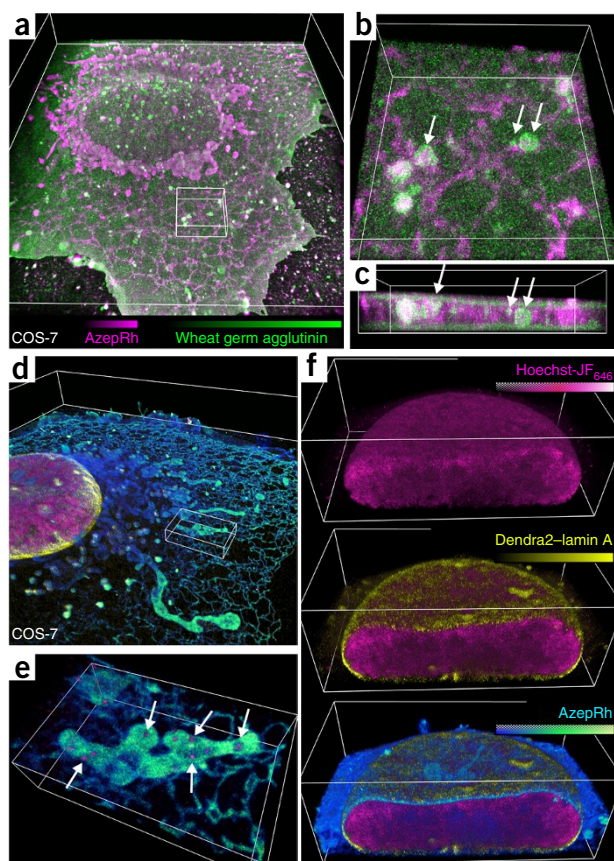

Figure 3 | Multicolor LLS-PAINT microscopy. (**a**) Volume rendering of a COS-7 cell that has been sequentially stained with AzepRh and wheat germ agglutinin–Alexa Fluor 555 to label intracellular and plasma membranes, respectively. (**b**,**c**) Magnified perspective and orthogonal views of the region outlined in **a**. White arrows indicate internalized vesicles adjacent to the ER yet peripherally stained with wheat germ agglutinin. (**d**) Three-color PALM and PAINT imaging of DNA (Hoechst-JF$_{646}$, PAINT, magenta), the nuclear envelope (Dendra2–lamin A, PALM, yellow) and intracellular membranes (AzepRh, PAINT, cyan) in a COS-7 cell. (**e**) Magnified perspective view of the region outlined in **d**. White arrows highlight mitochondrial DNA nucleoids. (**f**) Cutaway views oriented perpendicular to the s-axis through the nucleus in **d**. Bounding boxes are 50 × 60 × 6.5 μm (**a**), 6 × 6 × 2.1 μm (**b**), 6 × 2.6 × 1.5 μm (**c**), 60 × 60 × 7.5 μm (**d**), 7 × 4.4 × 1.6 μm (**e**) and 21.7 × 13 × 7.5 μm (**f**). Also see **Supplementary Videos 5**–**8**.

Figure 4 | 3D architecture of membranes and chromosomes during mitosis. (**a**) Volume rendering of two dividing LLC-PK1 cells in prophase (bottom) and metaphase (top) labeled with Hoechst-JF$_{646}$ and AzepRh to visualize DNA and intracellular membranes, respectively. (**b**) Cutaway section midway through the metaphase cell in **a**. White arrows highlight tubules of ER that intercalate between the condensed chromosomes in the metaphase plate. (**c**) Cutaway section midway through the nucleus of the prophase cell in **a**. (**d**) 200-nm-thick *xy* orthoslice through the same data set as shown in **a**–**c**. (**e**) Magnified view of the region outlined in **d**. (**f,g**) Magnified views of the region outlined in **e** showing orthoslices 10 nm (**f**; *xy*) and 5 nm (**g**; *xz*) thick through a mitochondrion adjacent to the nuclear envelope. A ring-shaped nucleoid of mitochondrial DNA (magenta) is embedded adjacent to mitochondrial membranes (green). Dashed lines indicate the regions from which corresponding *xy* and *xz* orthoslices were made. Cutaway sections in **b** and **c** are orientated perpendicular to the *cz* axis. Bounding boxes are 46 × 47.5 × 18 µm (**a**). Scale bars, 3 µm (**d**), 1 µm (**e**) or 200 nm (**f,g**). Also see **Supplementary Videos 9–11** and **16** and **Supplementary Figure 20**.

(45,000 volumes, 34 million molecules) to label intracellular and plasma membranes, respectively. This combination allowed visualization of both dorsal and ventral plasma membranes, 3D membrane ruffles at the cell periphery, and internalized plasma-membrane lined vesicles that appeared docked to the tubular network of the ER (**Fig. 3a–c** and **Supplementary Videos 5** and **6**).

PAINT microscopy is also compatible with both diffraction-limited fluorescence and super-resolution PALM (photoactivated localization microscopy), which further extends the range of structures that can be visualized together. We transiently expressed lamin A coupled to photoconvertible Dendra2 to label the nuclear envelope. After fixation, we performed LLS-PALM imaging as described previously[10]. Once the population of Dendra2 molecules was exhausted (14,000 volumes, 5.7 million molecules), we performed PAINT imaging using a novel fluorogenic DNA stain, Hoechst-JF$_{646}$ (**Supplementary Fig. 8**) (32,800 volumes, 10.6 million molecules), followed by AzepRh (76,000 volumes, 85 million molecules) to label DNA and intracellular membranes, respectively (**Fig. 3d–f** and **Supplementary Videos 7** and **8**). This strategy revealed interactions between organelles and proteins that could not be determined with either method alone. Hoechst labeling revealed heterogeneous density variation within the cell nucleus that was surrounded by the nuclear lamin network. However, we also observed small clusters of Hoechst staining outside the nucleus that, after multicolor imaging with AzepRh, were revealed to reside within the aforementioned mitochondrial voids, suggesting that they were in fact mitochondrial DNA nucleoids (**Fig. 3e** and **Supplementary Video 7**).

3D architecture of membranes and chromosomes in mitosis

Adherent interphase cells have relatively flat aspect ratios. However, even adherent cells become thicker and more isotropic as they undergo mitosis. Thanks to the planar confinement of the illumination, we were able to acquire multicolor 3D LLS-PAINT images of LLC-PK1 cells in prophase, metaphase and telophase with approximate dimensions of 40 × 50 × 7 µm, 20 × 20 × 18 µm and 50 × 25 × 20 µm, respectively. We performed two-color PAINT imaging using either Hoechst-JF$_{646}$ (80,154 volumes, 57 million molecules) and AzepRh (112,000 volumes, 191 million molecules) (**Fig. 4** and **Supplementary Videos 9–11**) or wheat germ agglutinin–Alexa Fluor 555 (20,000 volumes, 38 million molecules) and a
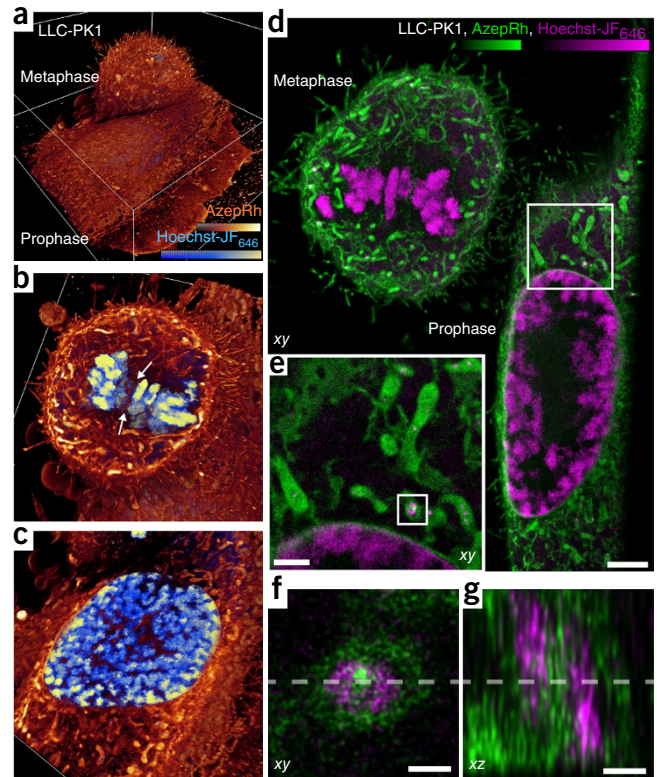
commercially available BODIPY-TR methyl ester dye (87,000 volumes, 379 million molecules) (**Supplementary Fig. 15** and **Supplementary Videos 12–14**) that stains intracellular membranes in a manner similar to AzepRh (**Supplementary Video 15**). Throughout the 20-µm thickness of the specimens, the LLS-PAINT images displayed substantially higher resolution than raw or deconvolved diffraction-limited LLS images with 260 × 260 × 730–nm resolution (for 560/580-nm excitation/emission) or LLS SIM-mode images with 170 × 260 × 320–nm resolution (**Supplementary Figs. 9** and **16** and **Supplementary Videos 9** and **12**). LLS-PAINT images were also superior to images from 3D widefield SIM with a theoretical resolution of 105 × 105 × 330 nm (as estimated by the cutoff of the optical transfer function) applied to a similar mitotic cell or from total internal reflection fluorescence SIM with a theoretical resolution of 96 × 96 nm applied to the peripheral region of a thin cell (**Supplementary Figs. 17–19** and **Supplementary Note 9**).

Dividing LLC-PK1 cells were densely covered with small, 1–3-µm-long × 0.2–0.4-µm-diameter membrane protrusions that were labeled at their periphery with wheat germ agglutinin and throughout their volume with AzepRh or BODIPY-TR methyl ester. In some samples, 10–20-µm-long retraction fibers anchored the cell to the coverslip (**Supplementary Fig. 15**). Hoechst-JF$_{646}$ labeled both nuclear and mitochondrial DNA (**Supplementary Videos 9** and **10**). Often we were able to observe complex-shaped nucleoids such as ring-shaped structures that resided within voids in the mitochondria (**Fig. 4d,e**). Close inspection revealed clear separation of the DNA and membrane signals at length scales of less than 100 nm (**Fig. 4f,g**, **Supplementary Fig. 20** and **Supplementary Video 16**). Metaphase chromosomes imaged via LLS-PAINT microscopy with Hoechst-JF$_{646}$ staining had rough surfaces with many 100–200-nm-long protrusions.

Figure 5 | 3D architecture of membranes in the zebrafish neuromast sensory organ. (**a**) Volume rendering of a neuromast on the lateral line of a 5-d-old zebrafish embryo labeled with AzepRh. Cutaway views oriented perpendicular to the *cz*-axis show the internal architecture at different depths within the organ. Several cell types and features can be identified. A central rosette of hair cells (HC) with dense mitochondrial staining appears immediately basal to the organ opening. This is surrounded by a layer of crescent cells (CC) and support cells (SC). Adjacent to the neuromast, lipid droplets (LD) and myofibrils (MF) are visible. (**b**) Left, 30-nm-thick orthoslices oriented perpendicular to either the *cz*- or the *s*-axis through the center of the neuromast. For comparison, deconvolved, diffraction-limited LLS orthoslices of the same regions are shown at right. Bounding box is 87.8 × 98.7 × 27.5 μm. A description of the image post-processing is presented in the Online Methods. Also see **Supplementary Videos 17** and **18**.
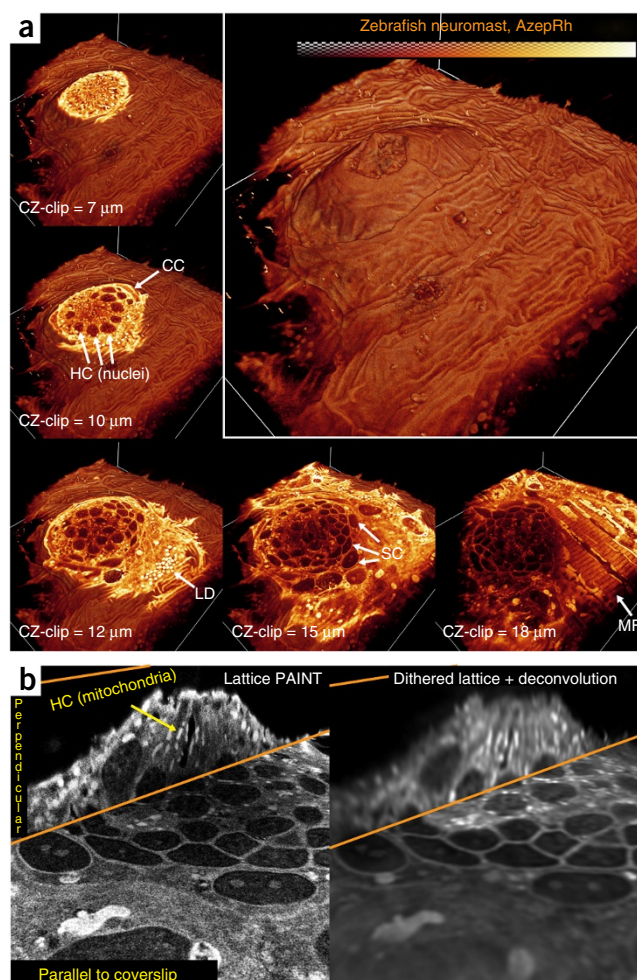

EM images of isolated, pre-swollen chromosome spreads show similar protrusions[27,28] that are thought to be composed of locally decondensed loops of chromatin. However, LLS-PAINT microscopy permits direct 3D visualization of these structures *in situ* in dividing cells, as well as in multicolor imaging of intracellular membranes (**Supplementary Fig. 21** and **Supplementary Videos 9–11**). ER structures, for example, formed a network of tubules that occasionally intercalated between chromosomes (**Fig. 4b**), although this apparent tubular architecture may also result from fixation-induced fenestration of cisternal sheets[29].

3D architecture of the zebrafish neuromast sensory organ

Although optical aberrations and label diffusion limit the depth attainable with the LLS-PAINT technique to ~20–30 μm, the microscope geometry does permit the study of the peripheral regions of much larger multicellular specimens to these depths. To illustrate, we performed LLS-PAINT imaging of a neuromast organ at the periphery of an intact zebrafish embryo using AzepRh (95,000 volumes, 1 billion molecules) (**Fig. 5** and **Supplementary Videos 17** and **18**). This organ consists of a rosette of hair cells surrounded by a layer of support cells. Kinocilia and stereocilia emerge from the hair cells and protrude through a circular opening in the periderm. The LLS-PAINT data set revealed multiple layers of cross-hatched striated muscle peripheral to the neuromast organ and interior to the outer layer of ridged periderm cells. In our sample, the kinocilia had flattened against the base, but we could also begin to resolve smaller stereocilia at the neuromast opening. Imaging deeper into the specimen revealed a rosette of approximately 15 hair cells with dense bundles of mitochondria that extended basally and radially away from the cuticular plate (**Fig. 5a**). Heterogeneous staining variations in hair cell and support cell nuclei (**Fig. 5a**) closely resembled condensed chromatin regions from electron tomography data sets[30], although it is uncertain whether AzepRh directly interacts with chromatin in zebrafish. Surrounding the hair cell rosette was a layer of support cells (**Fig. 5a**). In addition to higher resolution, the LLS-PAINT data set exhibited improved contrast compared to diffraction-limited deconvolved LLS images (**Fig. 5b**) owing to its superior optical sectioning, defined by the *z*-localization precision.

Compensation for nonlinear sample motion

PAINT microscopy is inherently performed under non-equilibrium conditions. If the labels bind permanently rather than transiently[31], which is likely to have been the case for the examples shown here, then the sample will be progressively perturbed as additional dye molecules bind. When imaged over many hours, our samples gradually swelled, and if left uncorrected, this swelling reduced the resolution of the final image (**Fig. 6**). Although this swelling is expected to occur with any exogenous labeling strategy, including heavy metal staining for EM, the deformation would not manifest during imaging because conventional super-resolution microscopy and EM are performed after labeling. Translational drift correction, common in localization microscopy using thin samples, is not sufficient to correct for the more complex nonlinear deformations exhibited by thicker 3D specimens in PAINT microscopy. In light of this, we used a combination of fiducial-based translational registration and nonlinear image transformation. We used a symmetric diffeomorphic image registration (SyN) algorithm, available through the open-source Advanced Normalization Tools (ANTs), which is commonly used for template generation and image registration in neuroscience[32]. With this, we registered sequential images plotted from time-integrated subportions of the total data to generate a spatiotemporally varying correction function (**Supplementary Note 10** and **Supplementary Figs. 22–25**). Although the improvement was more pronounced for the thicker 3D specimens, nonlinear swelling correction substantially increased image resolution in all data sets compared to no drift correction or translation-only drift correction (**Fig. 6** and **Supplementary Videos 19** and **20**).

Figure 6 | Compensation for nonlinear swelling in LLS-PAINT data sets. (**a**) A 60-nm-thick orthoslice oriented perpendicular to the *z*-axis through the dividing LLC-PK1 cell shown in **Supplementary Figure 15** that has been corrected for spatially invariant translational drift as well as nonlinear swelling using the SyN algorithm. Fourier shell correlation (FSC) performed for the region outlined by the dashed box shows a shift in weighting toward higher spatial frequencies for the SyN-corrected data sets compared to those with no correction (NC) and translation-only correction (Trans). (**b**) 60-nm-thick orthoslices of the boxed region in **a** at various levels of displacement correction. Scale bars, 2 μm (**a**) or 1 μm (**b**).

DISCUSSION

By limiting the illumination volume and providing high labeling density, LLS-PAINT microscopy allows for sub-100-nm–resolution imaging of thick, densely crowded specimens, including dividing cells and features at the periphery of small embryos. Our simulations suggest that, because of the stochastic nature of localization microscopy, resolving a given spatial frequency can require a fivefold or greater increase in the number of localized molecules compared to what would be required according to the Nyquist criterion. This observation suggests that previously reported resolution values that assume a requirement of 1× Nyquist density might be overly optimistic[1,10,13–18], if the expectation is that such values will apply to all structures across the field of view in the absence of *a priori* knowledge about the spatial structure of the sample. It also illustrates the limitations of using fluorescent labels as surrogates to resolve an underlying structure to which the labels are bound. The endogenous expression levels of many target proteins might not support sampling of an underlying structure at high spatial resolution, even if every protein molecule of a specific type can be labeled and localized. This might explain why prototypical localization microscopy data sets often focus on a few structural proteins that are normally found at very high densities, such as cytoskeletal components (e.g., actin and tubulin), focal adhesions (e.g., vinculin and paxillin) and endocytic pits (e.g., clathrin and caveolin). Further, it suggests that PAINT microscopy using labels targeted to lipids can enable higher resolution than localization microscopy techniques that target a specific protein, and it might point out an intrinsic limitation of protein engineering that would be shared even by EM methods using protein-specific contrast[33,34]. Further discussion on the design criteria for new PAINT probes to target additional structures is presented in **Supplementary Note 8**.

An obvious corollary is that the need for high localization density over a large, densely crowded 3D volume requires an enormous number of localization events with a substantial acquisition time. Many of the data sets presented here comprise more than 100,000 3D volumes, each consisting of approximately 100 2D image planes. At an exposure time of 25 ms per image, this translates to a volumetric imaging rate of 0.4 Hz, resulting in a total imaging duration of approximately 69 h. Serial labeling of multiple targets increases this time further. Thus it is not uncommon for acquisition of a single multicolor data set to take approximately 3–10 d. Although this is substantially slower than the imaging rates reported for 2D localization microscopy at comparable reported resolution[14], it is similar to the acquisition rate reported elsewhere for high-density 3D localization microscopy[18] when normalized to the number of focal planes and thus the imaging volume acquired. Ultimately, the volumetric imaging rate for LLS-PAINT
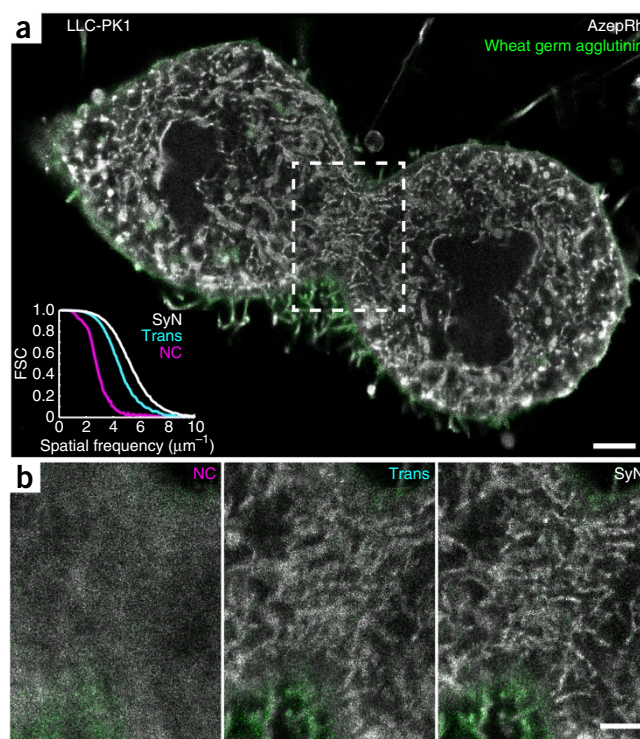
microscopy is limited by the rate of dye diffusion into the specimen (**Supplementary Fig. 26**).

Despite the long acquisition times, membrane-binding PAINT molecules such as AzepRh and BODIPY-TR methyl ester can have an important role in correlative microscopy when used in conjunction with protein-specific super-resolution methods such as PALM. For example, these dyes could eliminate the need for EM contrast agents that have deleterious effects on fluorescent labels and for the mechanical sectioning associated with EM of larger specimens, which can lead to sample distortion. Moreover, PAINT-PALM correlation occurs in the same instrument, without the need to remove the specimen and relocate the original field of view. Indeed, live-cell 3D imaging of cellular dynamics can be recorded with the LLS microscope immediately before *in situ* fixation and subsequent 3D PAINT microscopy and/or PALM, enabling further correlation of dynamics and function with membrane and protein structure, or allowing fixation and subsequent super-resolution imaging to be synchronized with a specific event such as drug delivery or optogenetic stimulation.

METHODS

Methods and any associated references are available in the online version of the paper.

Note: Any Supplementary Information and Source Data files are available in the online version of the paper.

Reprints and permissions information is available online at http://www.nature.com/reprints/index.html.

1. Sauer, M. Localization microscopy coming of age: from concepts to biological impact. *J. Cell Sci.* **126**, 3505–3513 (2013).
2. Betzig, E. *et al.* Imaging intracellular fluorescent proteins at nanometer resolution. *Science* **313**, 1642–1645 (2006).
3. Huang, B., Wang, W., Bates, M. & Zhuang, X. Three-dimensional super-resolution imaging by stochastic optical reconstruction microscopy. *Science* **319**, 810–813 (2008).
4. Shtengel, G. *et al.* Interferometric fluorescent super-resolution microscopy resolves 3D cellular ultrastructure. *Proc. Natl. Acad. Sci. USA* **106**, 3125–3130 (2009).
5. Huang, B., Jones, S.A., Brandenburg, B. & Zhuang, X. Whole-cell 3D STORM reveals interactions between cellular structures with nanometer-scale resolution. *Nat. Methods* **5**, 1047–1052 (2008).
6. Hajj, B. *et al.* Whole-cell, multicolor superresolution imaging using volumetric multifocus microscopy. *Proc. Natl. Acad. Sci. USA* **111**, 17480–17485 (2014).
7. Vaziri, A., Tang, J., Shroff, H. & Shank, C.V. Multilayer three-dimensional super resolution imaging of thick biological samples. *Proc. Natl. Acad. Sci. USA* **105**, 20221–20226 (2008).
8. York, A.G., Ghitani, A., Vaziri, A., Davidson, M.W. & Shroff, H. Confined activation and subdiffractive localization enables whole-cell PALM with genetically expressed probes. *Nat. Methods* **8**, 327–333 (2011).
9. Cella Zanacchi, F. *et al.* Live-cell 3D super-resolution imaging in thick biological samples. *Nat. Methods* **8**, 1047–1049 (2011).
10. Chen, B.C. *et al.* Lattice light-sheet microscopy: imaging molecules to embryos at high spatiotemporal resolution. *Science* **346**, 1257998 (2014).
11. Demmerle, J., Wegel, E., Schermelleh, L. & Dobbie, I.M. Assessing resolution in super-resolution imaging. *Methods* **88**, 3–10 (2015).
12. Deschout, H. *et al.* Precisely and accurately localizing single emitters in fluorescence microscopy. *Nat. Methods* **11**, 253–266 (2014).
13. Holden, S.J., Uphoff, S. & Kapanidis, A.N. DAOSTORM: an algorithm for high- density super-resolution microscopy. *Nat. Methods* **8**, 279–280 (2011).
14. Huang, F. *et al.* Video-rate nanoscopy using sCMOS camera-specific single-molecule localization algorithms. *Nat. Methods* **10**, 653–658 (2013).
15. Jones, S.A., Shim, S.H., He, J. & Zhuang, X. Fast, three-dimensional super-resolution imaging of live cells. *Nat. Methods* **8**, 499–508 (2011).
16. Shim, S.H. *et al.* Super-resolution fluorescence imaging of organelles in live cells with photoswitchable membrane probes. *Proc. Natl. Acad. Sci. USA* **109**, 13978–13983 (2012).
17. Shroff, H. *et al.* Dual-color superresolution imaging of genetically expressed probes within individual adhesion complexes. *Proc. Natl. Acad. Sci. USA* **104**, 20308–20313 (2007).
18. Xu, K., Babcock, H.P. & Zhuang, X. Dual-objective STORM reveals three-dimensional filament organization in the actin cytoskeleton. *Nat. Methods* **9**, 185–188 (2012).
19. Li, D. *et al.* Extended-resolution structured illumination imaging of endocytic and cytoskeletal dynamics. *Science* **349**, aab3500 (2015).
20. Sharonov, A. & Hochstrasser, R.M. Wide-field subdiffraction imaging by accumulated binding of diffusing probes. *Proc. Natl. Acad. Sci. USA* **103**, 18911–18916 (2006).
21. Fitzgerald, J.E., Lu, J. & Schnitzer, M.J. Estimation theoretic measure of resolution for stochastic localization microscopy. *Phys. Rev. Lett.* **109**, 048102 (2012).
22. Svitkina, T.M. & Borisy, G.G. Arp2/3 complex and actin depolymerizing factor/cofilin in dendritic organization and treadmilling of actin filament array in lamellipodia. *J. Cell Biol.* **145**, 1009–1026 (1999).
23. Nieuwenhuizen, R.P. *et al.* Measuring image resolution in optical nanoscopy. *Nat. Methods* **10**, 557–562 (2013).
24. Grimm, J.B. *et al.* A general method to improve fluorophores for live-cell and single-molecule microscopy. *Nat. Methods* **12**, 244–250 (2015).
25. Fiolka, R., Shao, L., Rego, E.H., Davidson, M.W. & Gustafsson, M.G. Time-lapse two-color 3D imaging of live cells with doubled resolution using structured illumination. *Proc. Natl. Acad. Sci. USA* **109**, 5311–5315 (2012).
26. Shao, L., Kner, P., Rego, E.H. & Gustafsson, M.G. Super-resolution 3D microscopy of live whole cells using structured illumination. *Nat. Methods* **8**, 1044–1046 (2011).
27. Ris, H. Stereoscopic electron microscopy of chromosomes. *Methods Cell Biol.* **22**, 77–96 (1981).
28. Harrison, C.J., Allen, T.D., Britch, M. & Harris, R. High-resolution scanning electron microscopy of human metaphase chromosomes. *J. Cell Sci.* **56**, 409–422 (1982).
29. Lu, L., Ladinsky, M.S. & Kirchhausen, T. Cisternal organization of the endoplasmic reticulum during mitosis. *Mol. Biol. Cell* **20**, 3471–3480 (2009).
30. Owens, K.N. *et al.* Ultrastructural analysis of aminoglycoside-induced hair cell death in the zebrafish lateral line reveals an early mitochondrial response. *J. Comp. Neurol.* **502**, 522–543 (2007).
31. Jungmann, R. *et al.* Multiplexed 3D cellular super-resolution imaging with DNA-PAINT and Exchange-PAINT. *Nat. Methods* **11**, 313–318 (2014).
32. Avants, B.B., Epstein, C.L., Grossman, M. & Gee, J.C. Symmetric diffeomorphic image registration with cross-correlation: evaluating automated labeling of elderly and neurodegenerative brain. *Med. Image Anal.* **12**, 26–41 (2008).
33. Martell, J.D. *et al.* Engineered ascorbate peroxidase as a genetically encoded reporter for electron microscopy. *Nat. Biotechnol.* **30**, 1143–1148 (2012).
34. Shu, X. *et al.* A genetically encoded tag for correlated light and electron microscopy of intact cells, tissues, and organisms. *PLoS Biol.* **9**, e1001041 (2011).

ONLINE METHODS

Instrumentation. We performed all experiments at room temperature on a previously described LLS microscope[10]. We made several modifications to accommodate the 3D PAINT experiments. First, to perform axial localization via astigmatism[3,35], we mounted a cylindrical lens with a focal length of 1,000 mm (ThorLabs, J1516RM-A) approximately 40 mm from the camera sensor. Second, we used a 2-W 560-nm continuous wave laser (MPB Communications, 2RU-VFL-P-2000-560-B1R) to increase illumination intensities at the sample and thus increase the imaging speed. Because of losses within the optical system, incident powers were in the range of 5–25 mW into the back pupil of the excitation objective. Complete experimental details for each data set including illumination power (as measured at the back pupil of the excitation objective and estimated at the sample), exposure time per 2D image, number of 2D images per volume and number of volumes per data set are available in **Supplementary Table 1**. Finally, to compensate for evaporation and to maintain dye concentration throughout an experiment, we continuously perfused buffer from an approximately 1–2-l reservoir through the sample bath using a peristaltic pump (Warner Instruments, Model 720). PAINT label concentration varied among samples and labels but was generally between 100 pM and 1 nM in phosphate-buffered saline (PBS). Documentation for the construction of a copy of the LLS microscope is freely available after execution of a research license with Howard Hughes Medical Institute (HHMI). Researchers can also apply to access the microscope as visitors through the Advanced Imaging Center at Janelia Research Campus (https://www.janelia.org/aic).

Sample preparation. We pre-cleaned 5-mm-diameter coverslips (Warner Instruments, CS-5R) by immersing them in 1 M KOH for 1 h and then in de-ionized water for 1 h, both under sonication. We dried the coverslips and heated to them 100 °C on a hotplate. We then deposited 10 μl of a 1:100 dilution of stock solution of 50-nm gold nanorods (Nanopartz, A12-50-600-25) to 200 proof EtOH onto each coverslip and allowed to evaporate. We then sputtered 40 nm of SiO_2 onto the coverslips using a Denton Explorer (Denton Vacuum). The approximate density of fiducial markers ranged between 5 and 25 per 100×100 μm field of view. We obtained COS-7 cells from ATCC. We obtained LLC-PK1 cells as a gift from Dr. Mike Davidson at Florida State University. We maintained all cell lines in Dulbecco's modified Eagle's medium + 10% FBS and verified that they were free of mycoplasma. Before plating cells, we UV-sterilized coverslips and coated them with 10 μg/ml fibronectin (Millipore, FC010) for 1 h to aid adhesion before rinsing them with sterile PBS. After 24–48 h we fixed cells for 1 h at room temperature using a solution of 4% paraformaldehyde (Electron Microscopy Sciences), 0.1% glutaraldehyde (Electron Microscopy Sciences) in PHEM buffer (25 mM HEPES, 10 mM EGTA, 2 mM $MgCl_2$, and 60 mM PIPES, all from Sigma-Aldrich). Before fixation, we transfected the cell shown in **Figure 3** with Dendra2–lamin A as described previously[10]. We purchased BODIPY-TR methyl ester from Life Technologies (C34556). Zebrafish experiments were conducted according to protocols approved by the Institutional Animal Care and Use Committee of the Howard Hughes Medical Institute, Janelia Research Campus. To image the neuromast organ, we anesthetized 5-d-old Casper zebrafish embryos[36] in MS-222 and fixed them in 4% paraformaldehyde in PBS overnight at 4 °C with gentle agitation on a rocker. After fixation, we embedded the fish in a thin layer of 1% low-melting-point agarose with a 1:5 dilution of stock solution 50-nm gold nanorods. We aspirated excess agarose to leave only a very thin (~1 μm) layer surrounding the neuromast structures.

Single-molecule localization and image characterization. We stored individual volumes as multipage TIFF stacks and imported them into Matlab (Mathworks) for further analysis. We identified fluorescent molecules as local maxima in a Gaussian-filtered version of each 2D image, and we fit the raw, photon-converted data from each molecule to a generalized elliptic 2D Gaussian via Levenberg-Marquardt optimization. We linked sequential localizations of the same molecule into a single higher-accuracy localization using a spatiotemporal cutoff filter. We performed all optimization on a graphics processing unit (GPU; NVIDIA GeForce GTX Titan) using custom-written CUDA code called via a Matlab mex function. Full details of the numerical procedure are provided in **Supplementary Note 11**. For each data set, we report the mean number of photons detected for each molecule; the number of molecules per 100-nm cubic volume; the x, y and z localization precision; and the lower bounds on the x, y and z image resolution as a function of the spatial coordinates in the image. These data represent a thorough characterization of each experiment and are presented in **Supplementary Videos 4**, **6**, **8**, **11**, **14** and **18**. For reference, when these movies are opened in Quicktime, individual frames can be manually selected for fuller viewing of the data. Additional statistics and histograms regarding the localizations for each data set are provided in **Supplementary Figure 27**.

Fourier ring correlation and Fourier shell correlation represent the relative weighting of spatial frequencies in an image. Thus, if the underlying sample remains the same, a shift in the Fourier ring or shell correlation of an image toward higher spatial frequencies can reveal the beneficial effects of drift correction. We computed the Fourier shell correlation comparison (in **Fig. 6**) according to previously outlined methods[23]. We point out here that although this metric is useful for analyzing changes in resolution that occur through transformations to or by incorporating additional localizations within the same sample, care should be taken when using this method as an absolute metric for comparing the spatial resolution between images of different labels or structures (**Supplementary Fig. 28**). Further discussion is provided in **Supplementary Note 4**.

Code availability. All the data in the manuscript are available upon request, including high-resolution, 3D images and the raw localization statistics. Software for identifying, localizing and plotting single-molecule data is freely available after execution of a research license with HHMI. The ANTs software for image registration is freely available from http://stnava.github.io/ANTs/.

Image rendering. We plotted 3D localization microscopy images either by rendering each individual molecule as a 3D Gaussian probability distribution (for 2D slice representation) or by generating a 3D super-resolution histogram and smoothing the final image with a Gaussian kernel (for volume renderings). For certain data sets, we applied gamma correction to more clearly illustrate

fine-scale structures. Two data sets also underwent additional rescaling before display. First, the fixation buffer used for the COS-7 cell displayed in **Figure 2** was contaminated with microbial debris. This debris was visible in the reconstructed data set and obscured the intracellular structures of interest when images were displayed as a maximum-intensity projection. Therefore, before image rendering, we masked structures exterior to the cell with a user-generated binary image filter. Second, the periphery of the zebrafish neuromast data set in **Figure 5** showed greater numbers of localizations, and thus higher contrast, than interior regions. To more clearly illustrate features within the hair cell rosette, we normalized the contrast between interior and peripheral regions using contrast-limited adaptive histogram equalization via the CLAHE plugin in Fiji[37]. For comparison purposes, the resolution

characterization images of these data sets in **Supplementary Videos 4** and **18** show the full, unprocessed data. We plotted final images as 3D matrices in Matlab and exported them in NifTI format using the "NifTI tools" toolbox from the Matlab File Exchange. We then imported NifTI images into Amira (FEI) or Fiji for visualization, image rendering and video generation.

35. Kao, H.P. & Verkman, A.S. Tracking of single fluorescent particles in three dimensions: use of cylindrical optics to encode particle position. *Biophys. J.* **67**, 1291–1300 (1994).
36. White, R.M. *et al.* Transparent adult zebrafish as a tool for in vivo transplantation analysis. *Cell Stem Cell* **2**, 183–189 (2008).
37. Schindelin, J. *et al.* Fiji: an open-source platform for biological-image analysis. *Nat. Methods* **9**, 676–682 (2012).